Channel Impulse Analysis of Light Propagation for Point-to-Point Nano Communications Through Cortical Neurons

Stefanus Wirdatmadja, Josep Miquel Jornet, *Member, IEEE*, Yevgeni Koucheryavy, *Senior Member, IEEE*, and Sasitharan Balasubramaniam, *Senior Member, IEEE*

***Abstract*— Recent Brain-Machine Interfaces have moved towards miniature devices that can be seamlessly integrated into the cortex. In this paper, we propose communication between miniature devices using light. A number of challenges exist using nanoscale light-based communication and this includes diffraction, scattering, and absorption, where these properties result from the tissue medium as well as the cell's geometry. Under these effects, the paper analyses the propagation path loss and geometrical gain, channel impulse and frequency response through a line of neurons with different shapes. Our study found that the light attenuation depends on the propagation path loss and geometrical gain, while the channel response is highly dependent on the quantity of cells along the path. Additionally, the optical properties of the medium impact the time delay at the receiver and the width and the location of the detectors. Simulations were conducted for cells that are lined horizontally up to a distance of 450 μm using light wavelength of 456 nm and different neuron densities (men's neocortex (25 924($\pm$15 110) /mm^3) and women's (27 589($\pm$16 854) /mm^3)). Based on the simulations, we found that spherical cells attenuate approximately 20% of the transmitted power compared to the fusiform and pyramidal cells (35% and 65%, respectively).**

***Index Terms*— Nano communications, optogenetics, light propagation modelling, neural systems.**

I. Introduction

IMPLANTABLE medical devices in recent years have witnessed an exponential growth due largely to numerous supporting fields, including nanotechnology, computer science, and electrical engineering. The advancements in such fields are leading to miniature devices, constructed from biocompatible materials and powered by means of energy-harvesting systems, which can be permanently implanted. In this context, the emerging field of nano-communications is aimed at enabling the exchange of information and coordination between nano-devices. Two approaches for nano-communications have been developed in parallel, namely, nano-electromagnetic (EM) communications [1] and molecular communications [2]. A number of works have looked at molecular communications for neural systems. For example, [3] conducts and analyzes in-vivo information transfer on the nervous system of an earthworm, [4] proposes the complete synaptic communication channel model, and [5] investigates the upper bound for neural synaptic communication. Acoustic signals have been proposed to allow devices to communicate [6], but the unit circuitry may be larger than the envisioned micron-scale size devices that needs to be placed deep in the tissue. This challenge is further exacerbated when we consider implanting the devices in the cortex of the brain. In the case of nano-EM communications, a major challenge is the selection of an appropriate frequency for signaling that is relative to the size of the antenna components. This is because the reduction in size of an antenna means that the operating frequency also increases [1], and THz waves are unable to penetrate through biological tissues. This is due to the high energy photons interacting with living cells at the molecular scale through the process of absorption [7], [8]. This means that other modes of communication are required in order to enable devices to communicate and network in biological tissues.

In our previous work [9] a miniature device known as Wireless Optogenetic Nano Devices (WiOptND) for neural stimulation was proposed. The device utilizes ultrasound signals for energy harvesting to produce power for a light source that is used for stimulating small population of neurons, and this process is known as optogenetics. Some constraints in optogenetics stimulation are investigated in [10] in terms of distortion from the spike generation delay due to the stochastic behaviour of the surface receptors, which results in random time response delays from the time a neuron is externally stimulated. In other works, light has been used to communicate between devices through red blood cells [7]. While both THz waves and optical signals are very high frequency EM waves, one key difference is that the latter does not suffer from strong

Manuscript received October 30, 2019; revised April 29, 2020 and July 17, 2020; accepted July 21, 2020. Date of publication July 28, 2020; date of current version November 18, 2020. The work has been supported by Science Foundation Ireland (SFI) FutureNeuro (16/RC/3948) and CONNECT (13/RC/2077) Research Centres, National Science Foundation under Grant CBET-1706050, as well as the Academy of Finland under Grant 284531. The associate editor coordinating the review of this article and approving it for publication was W. Shieh. *(Corresponding author: Sasitharan Balasubramaniam.)*

Stefanus Wirdatmadja and Yevgeni Koucheryavy are with the Department of Electronic and Communication Engineering, Tampere University, 33720 Tampere, Finland (e-mail: stefanus.wirdatmadja@tuni.fi; evgeny.kucheryavy@tuni.fi).

Josep Miquel Jornet is with the Department of Electrical and Computer Engineering, Northeastern University, Boston, MA 02115 USA (e-mail: jmjornet@northeastern.edu).

Sasitharan Balasubramaniam is with the Telecommunication Software and Systems Group, Waterford Institute of Technology, Waterford, X91 K0EK Ireland (e-mail: sasib@tssg.org).

Color versions of one or more of the figures in this article are available online at http://ieeexplore.ieee.org.

Digital Object Identifier 10.1109/TCOMM.2020.3012477

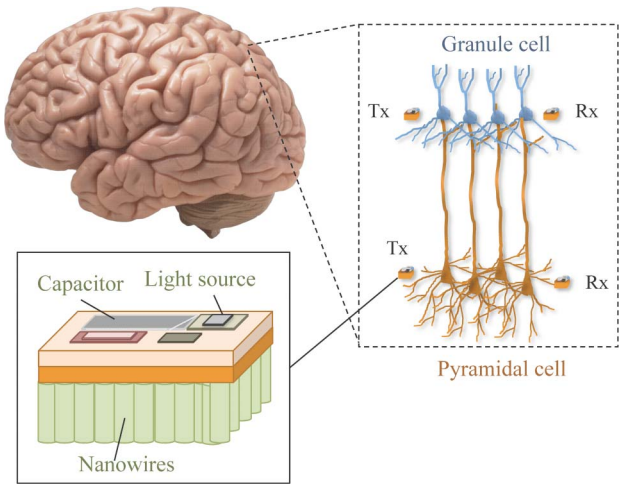

Fig. 1. Illustration of the Wireless Optogenetic Nanodevice (WiOptND) network that are placed within the cortex. The communication between the devices is established using light that penetrates through the cells.

absorption compared to the former due to tissue water content. In recent years, extensive modelling has been established for behaviour of light that is used for stimulating neurons, but there have not been any proposal towards using nanoscale light communication between devices implanted into the brain. While optical signals suffers from scattering phenomenon, this does not directly translate into undesired effects since it also supports the light focusing phenomenon during the propagation process through neurons, which we found in our previous study [11]. In this paper, we propose communication between the WiOptND devices using light. As illustrated in Fig. 1, this could lead to miniature nanonetworks that are implanted into the brain cortex, and the communication and cooperation between the WiOptNDs can enable neural circuit stimulation of different micro-columns within the cortical cortex that have impaired connections.

A major challenge with light communication through neural tissue, and in particular at micron-scale, is that the propagation of the light is largely determined by the physiological shape as well as the organelles within the cell. This is due to the size of the source that produces light waves that are comparable to the size of the neuron. Therefore, the propagation behaviour of the light is largely dictated by the composition of the tissue. Neural tissue is composed of cells with different physiological properties, each of which contributes differently towards the propagation pattern. In this paper, we focus on the power delay profile, femto-pulse signal analysis in both time and frequency domains, and the channel impulse response of light propagation for physical communication analysis in neural tissue. We employ a ray tracing approach to analyze the light propagation along the path of cells in the neural tissue, due to the scale of the light source being comparable to the size of the soma of the neurons, which allows us to model the propagation of individual rays spatially to understand how the shapes of the cell will influence their propagation. Additionally, when the ray tracing is combined with the modified Beer-Lambert accounting for absorption and scattering, the intensity attenuation can be computed accurately. While a Finite Difference Time Domain (FDTD) solver can increase the accuracy of the result with all available parameters, solving Maxwell's equations is much more computationally demanding that utilizing ray tracing methods. Our aim is to determine the channel impulse response of the light signal as it propagates through different shapes as well as density of neurons. We extend the discussion in [11] and [12] in terms of fundamental propagation medium characterisation and its effect on a single line array of cells, which can affect the communication performance between two WiOptNDs devices that are communicating with each other using light. Moreover, we derived the impulse responses based on the cell's morphology, which is an analysis that is beneficial for determining the light propagation behaviour that can impact on the communication performance. The contributions of this paper are as follows:

- **Geometric Analysis of Light Propagation and Path Loss Analysis:** We derive the total path loss formula for three different neuron geometries, namely fusiform, spherical, and pyramidal based on optical properties of the brain tissue and neurons. We analyze the focusing gain for multiple-(radial-based)-cell light propagation that results from the converging and diverging light phenomena through the array of cells.
- **Numerical Analysis of Channel Impulse Response for Light Propagation:** We define a channel impulse response model based on the physiological shapes of the aforementioned neurons. This includes numerical analysis to determine the impact of light propagation through a line of neurons to determine how this impacts on the impulse response. The approach taken is through multiple ray tracings that simulates individual rays as they propagate through the array of cells.

This paper is organized as follows: In Sec. I, we present the background and motivation of this paper. In Sec. II, we elaborate the light absorption and scattering phenomena in biological tissue. In Sec. III, we derive the total path loss for three geometric neuron models. In both Sec. IV and V, we analyze the simulated system in both time and frequency domains. In Sec. VI, we elaborate the results based on the simulated light propagation system and relate them with the geometrical and optical properties of the system. Finally, we present the conclusion in Sec. VII.

II. Absorption and Scattering in Biological Tissue

In general, for all cell geometries, the path loss is determined by the medium in which the light traverses. In our case, the medium consists of biological tissues that contains neural cells. Each propagation medium has three significant parameters that play a role in the behaviour of light transmission, namely absorption coefficient (μ_a), reduced scattering coefficient (μ_s') which indicates random photon path exists due to scattering, and distance (d) between the transmitter and the receiver [13], [14]. The last parameter is heavily dependent on the refraction of light as it propagates through the medium, which is governed by the cell's geometry and the refractive index of different internal components (n) of the organelles.

The propagation medium investigated in this paper consists of two biological mediums with different optical parameters. The two mediums are the brain tissue and each individual neuron. The brain tissue comprises many components including neuroglia and astrocytes, while neuron consists of cytoplasm, mitochondria, nucleus, and many other organelles. In this work, we consider that the absorption coefficients remain constant for each medium throughout the propagation path. Additionally, these mediums are modeled as homogeneous materials for computational tractability. Moreover, since the distance is very short between the homogeneous cells, the effect of other components is negligible on the scattering. However, the scattering between the cells is still considered by representing the tissue scattering coefficient as the average value of those scatterers. Therefore, the path loss analysis is based on the propagation distance, where the distance determines how the medium changes impact on the light path. The light intensity along the propagation path for each medium is analyzed using the modified *Beer-Lambert law* and is represented as [15], [16], [17],

$$I(\lambda, d) = I_0(\lambda) e^{-\mu_a(\lambda) d DPF(\lambda, d)}, \tag{1}$$

where $I(\lambda)$ is light intensity at λ wavelength on distance d, $I_o(\lambda)$ is the light intensity at the source, and $DPF(\lambda, d)$ is the Differential Path Length Factor, which is a scaling factor indicating the distance traveled by the light wave that is impacted by the shifted direction due to the interaction with the neuron (please note that our light source is at nanoscale and will, therefore, be highly impacted by the cell shape).

The DPF is the element which is included in the modified *Beer-Lambert* law and is affected by the optical medium properties, namely the absorption (μ_a) and the reduced scattering (μ_s') coefficients [18], and is represented as follows

$$DPF^{(k)}(\lambda, d) = \frac{1}{2}\left(\frac{3\mu_s'(\lambda)}{\mu_a(\lambda)}\right)^{1/2}\left[1 - \frac{1}{1 + d(3\mu_a(\lambda)\mu_s'(\lambda))^{1/2}}\right]. \tag{2}$$

The propagation channel elaborated in this paper consists of two mediums (cell and brain tissue) which are categorized as intra and inter-cell propagation mediums. Therefore, the DPF equation (2) should be applied to all paths with respect to its medium.

Based on (1) and (2), the medium light transmittance $T(\lambda, d)$ can be represented as

$$T(\lambda, d) = \frac{I(\lambda, d)}{I_0(\lambda)} = e^{-\mu_a(\lambda) d DPF(\lambda, d)}. \tag{3}$$

III. Geometric Model of Multiple Cell Path Loss

Along with other aspects such as cell organelles and the size ratio between a cell and a light wavelength, the geometry of the cell has a significant effect on the light propagation behaviour as discussed in Sec. I, and this is largely due to the size and aperture of the light source, and attenuation of the intensity. The geometrical analysis for the physiological shapes of the neurons is based on the models in [11], and the three different neurons that is analyzed in this paper are *Fusiform*, *Spherical*, and *Pyramidal* cells. In addition to the shape and size of each individual neuron, the light wave traverses a dense neural population. In this section, we elaborate the effect by the cell's geometry on the light propagation as it traverses a line of neurons that are of the same type.

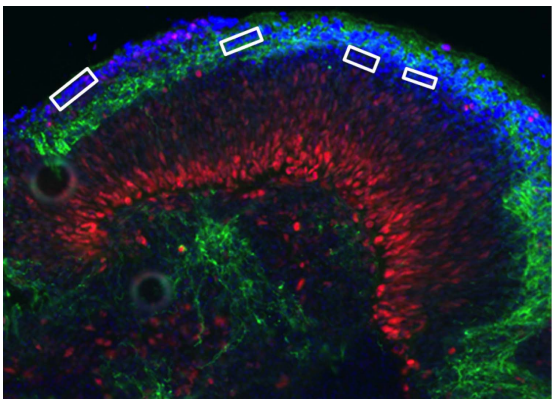

Fig. 2. Image of a 5-week old induced Pluripotent Stem Cells (iPSC) cerebral organoid with differentiated neurons [19]. The white box illustrates examples of dense cells that are arranged in a straight line.

Neurons that are densely packed can be structured in a straight line and examples of this is illustrated in Fig. 2. The figure shows an induced Pluripotent Stem Cell (iPSC) brain organoid with differentiated neurons, where the white boxes illustrates examples of spherical neurons that are in a straight line (this is based on experiments we have conducted in our past work [19]). Each cortical layer of the neocortex is populated by various types and ratio of neurons. For example, pyramidal cells are usually found in layers III and V, while fusiform cells are located in layer VI [20]. Additionally, the average neuron density in men's neocortex is 25,924($\pm$15,110) /mm^3 and women's is 27,589($\pm$16,854) /mm^3 [21]. Therefore, by considering that our device will only communicate through a line of homogeneous cells within the layers of the neocortex, the general formula for the total path loss in dB for N number of any given shape of neurons is represented as

$$\begin{aligned} PL_{total} = 4.343\Big[&N\mu_a^{(c)}(\lambda)\overline{d_a}DPF(\lambda, \overline{d_a}) \\ &+ (N-1)\mu_a^{(u)}(\lambda)\overline{d_e}DPF(\lambda, \overline{d_e}) \\ &+ \mu_a^{(u)}(\lambda)(d_E + d_R)DPF(\lambda, (d_E + d_R))\Big], \end{aligned} \tag{4}$$

where $\overline{d_a}$ and $\overline{d_e}$ are the average propagation distances in a cell and between two cells based on its shape, respectively, d_E and d_R are the distances of the light source from the first cell and the location of the receiver from the last cell, respectively. The superscript (c) or (u) indicates whether the parameter belongs to the cell or brain tissue.

In the following subsections, we present the derivation for both $\overline{d_a}$ and $\overline{d_e}$ for the three different types of neurons, where they are cholinergic neurons that are found in the cerebral cortex [20]. The shapes for each of the cells, as well as the geometric analysis of light propagation through the tissue is illustrated in Fig. 3.

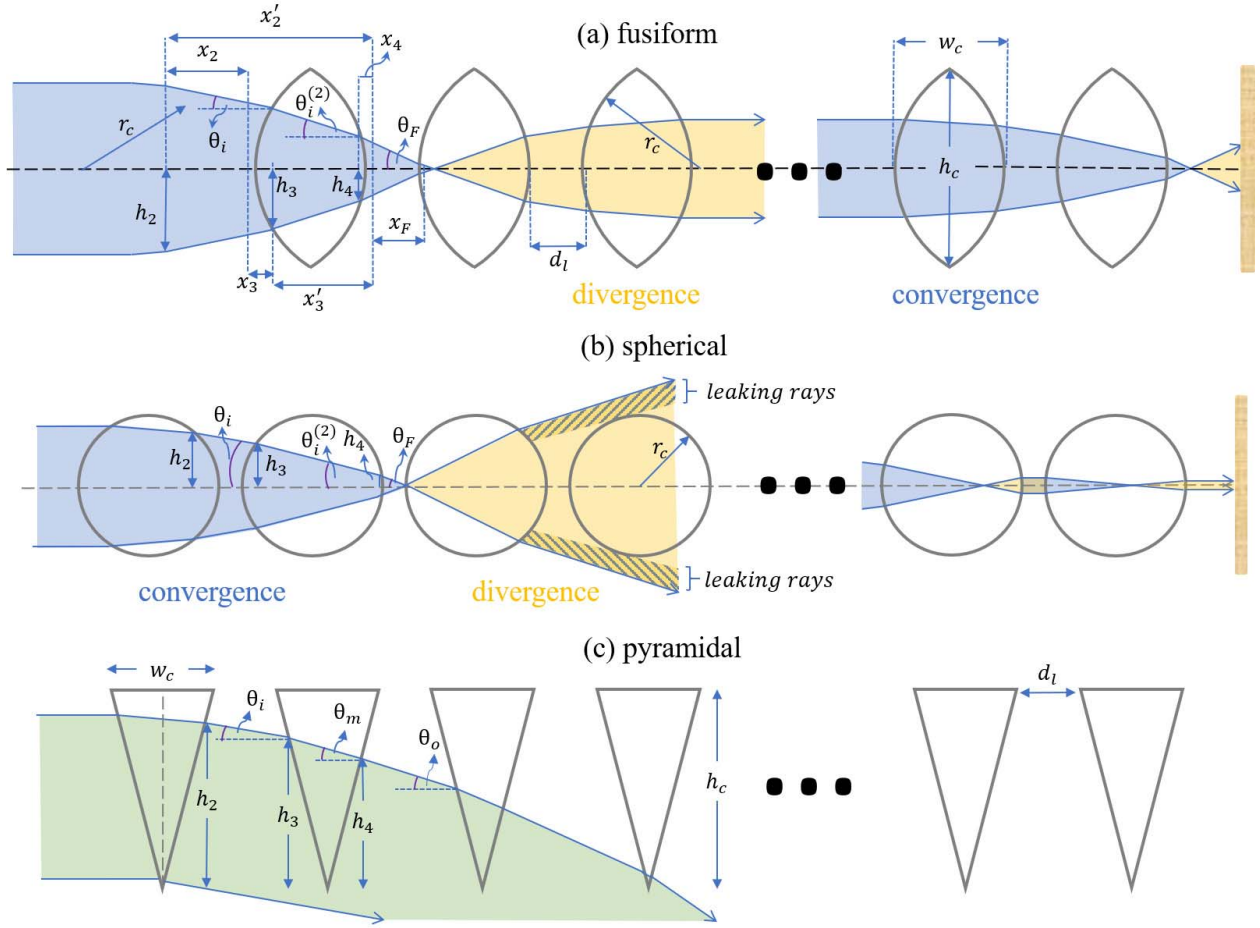

Fig. 3. Geometrical analysis of light propagation using ray tracing as it propagates through a one-dimensional array of neurons, and this includes (a) fusiform, (b) spherical, (c) pyramidal cells.

A. Fusiform Cell

A fusiform cell can be projected onto a 2D-plane as an oval or convex lens, as illustrated in Fig. 3(a). The dimensions of the cell are represented with a height h_c, width w_c, a surface curvature radius of r_c, and their relationship is represented as

$$r_c = \frac{{h_c}^2 + {w_c}^2}{4w_c}. \tag{5}$$

A single neuron of this shape has a focusing behaviour when collimated light propagates through the cell. To investigate the light propagation behavior for multiple neurons organized in a one-dimensional array, several fusiform cells are positioned in a sequence so that the collimated light propagates in a non-line-of-sight manner from the second cell. Applying this model to observe the focusing phenomena leads to another light behaviour which is the divergence effect. The divergence effect occurs when the focus point becomes shorter as the light propagates through consecutive fusiform cells. Due to the cell geometry, the focusing/converging and diverging phenomena occurs alternately, and this phenomena is illustrated in Fig. 3(a). Using geometrical analysis, the average propagation distances inside the fusiform cell d_a and between the cells d_e are formulated as

$$\begin{aligned}\overline{d_a} &= \frac{4}{h_c}\int_{\frac{r_c-h_c}{2}}^{\frac{r_c}{2}} \sqrt{{r_c}^2 - x^2} - (r_c - \frac{w_c}{2})dx \\ &= \frac{1}{6h_c}\Bigg[6h_c w_c - 12{r_c}^2 \arcsin\left(\frac{r_c - h}{2r_c}\right) \\ &\qquad + 3(h_c - r_c)\sqrt{3{r_c}^2 + 2h_c r_c - {h_c}^2} \\ &\qquad + \left(2\pi + \sqrt{27}\right){r_c}^2 - 12h_c r_c\Bigg],\end{aligned} \tag{6}$$

$$\begin{aligned}\overline{d_e} &= d_l + \frac{2}{h_c}\int_{\frac{r_c-h_c}{2}}^{\frac{r_c}{2}} \frac{w_c}{2} - \sqrt{{r_c}^2 - x^2}dx \\ &= d_l + \frac{1}{12h_c}\Bigg[-6h_c w_c + 12{r_c}^2 \arcsin\left(\frac{r_c - h_c}{2r_c}\right) \\ &\qquad + (3r_c - 3h_c)\sqrt{3{r_c}^2 + 2h_c r_c - {h_c}^2} \\ &\qquad + \left(-2\pi - \sqrt{27}\right){r_c}^2 + 24h_c r_c\Bigg].\end{aligned} \tag{7}$$

B. Spherical Cell

Fig. 3(b) illustrates a spherical shaped neuron with radius r_c projected onto a 2D space. The behaviour of the spherical

shaped cell is similar to the fusiform cell, and this is from the focusing effects. However, depending on the density of the neurons, the distance between the cells d_l has a significant role in *leaking* light rays which does not occur in multiple fusiform neural tissue. Leaking rays are the rays that do not propagate to the next adjacent cell. Therefore, they are not further transmitted along the propagation path. However, the alternating converging and diverging phenomena are similar for both spherical and fusiform cells. The light propagation for multiple spherical neurons in a 1-dimensional array is illustrated in Fig. 3(b). For the spherical cell the average propagation distance d_a inside a cell and between cells d_e is given by

$$\overline{d_a} = \frac{2}{r_c}\int_0^{r_c} \sqrt{r_c^2 - x^2}dx = \frac{1}{2}\pi r_c, \tag{8}$$

$$\overline{d_e} = d_l + \frac{1}{r_c}\int_0^{r_c} r_c - \sqrt{{r_c}^2 - x^2}dx = d_l - \frac{1}{4}(\pi - 4){r_c}^2. \tag{9}$$

Similar to the fusiform cell analysis, $\overline{d_a}$ and $\overline{d_e}$ of the spherical cells considers all the light rays along the propagation axis. However, the difference lies in the distance between the incoming and outgoing surfaces for the rays.

C. Pyramidal Cell

The propagation behaviour for pyramidal cells is significantly different when compared to the two aforementioned neurons in terms of light ray traces, and this is illustrated in Fig. 3(c). A pyramidal cell tends to deviate the light path due to the refraction of two different medium, and takes on a behaviour that is very similar to a prism. In this case, the light traversing through multiple pyramidal cells deviates from its initial axis before it completely propagates from the line path of the arrays of cells. The light deviation behaviour with respect to the cell's geometry is illustrated in Fig. 3(c). The average propagation distance d_a inside a cell and between cells d_e is represented as

$$\overline{d_a} = \frac{2}{h_c}\int_0^{h_c} \left[\frac{w_c}{h_c}(x - h_c) + \frac{w_c}{2}\right] dx = \frac{1}{2}w_c, \tag{10}$$

$$\overline{d_e} = d_l + \frac{1}{h_c}\int_0^{h_c} \left[\frac{w_c}{h_c}(x - h_c) + \frac{w_c}{2}\right] dx = d_l + \frac{1}{4}w_c. \tag{11}$$

The 2-D projection of the pyramidal cell can be perceived as an isosceles triangle, which is similar to a prism. Therefore, the light ray deviation angle is governed by the medium refraction indices. Both (10) and (11) include ray traces from inside a cell and between two neighbouring cells.

IV. Multi-Neuron Light Propagation Channel Impulse Response

The cell geometry and the tissue optical properties have a significant effect on the impulse response of the propagation channel. In this section, we derive how the geometrical analysis of the previous section plays a role on the channel impulse response, and how this differs between the three different types of neurons. The combination of both the cell's geometry and the optical properties results in attenuation as well as delay of the light propagation to the detector. This is largely due to the collimation as well as divergence due to the geometric shape and results in multiple propagation paths of the light rays.

The general expression of multipath impulse response considering N number of neurons that are placed in a 1-dimensional array can be formulated as [22]

$$h(t; d_{total}, \lambda) = \overset{N}{\underset{n=1}{\circledast}} h_a^{(n)}(t; d, \lambda) \circledast \overset{N+1}{\underset{n=1}{\circledast}} h_e^{(n)}(t; d, \lambda), \tag{12}$$

where $h^{(n)}(t; d, \lambda)$ represents the impulse response of the light ray corresponding to the n^{th} cell, λ is the wavelength, t is the time, and the corresponding subscript *a* or *e* indicates if it is an intra-cell or inter-cell propagation. Furthermore, the intercell impulse response, $h_e^{(n)}$ in (12), consists of three elements, $h_c^{(n)}$, h_E, and h_R, and is represented as follows

$$\overset{N+1}{\underset{n=1}{\circledast}} h_e^{(n)}(t; d, \lambda) = \overset{N-1}{\underset{n=1}{\circledast}} h_c^{(n)}(t; d^{(n)}, \lambda) \circledast h_E(t; d_E, \lambda) \circledast h_R(t; d_R, \lambda) \tag{13}$$

where subscripts *c, E*, and *R* indicates the propagation paths between the cells, light source, and the receiver (detector), respectively, d_E is the distance between the light source and the first cell, and d_R is the distance between the last cell and the receiver. As shown in (12), the impulse response is based on the convolution as the light propagates through each individual cell along the path, and the brain tissue between the cells.

The light source applied in this system is considered as a collimated light where the generated rays has equal intensity following the uniform distribution $\mathcal{U}(0, 1)$. In order to use the ray tracing model, the infinite rays should be discretized to *K* rays. Since the intensity parameter is used, the discretization process has no impact on the intensity value. To further elaborate on this, each intra and inter-cell propagation impulse response can be divided into two parts, namely, the attenuation component and the delay component. The attenuation follows the modified Beer-Lambert equation, while the delay can be expressed as a delta dirac function. Thus, the impulse response for k^{th}-path is represented as

$$h_a^{(k)}(t; d^{(k)}, \lambda) = I_E T_a^{(k)}(\lambda)\delta(t - t_a^{(k)}) \circledast I_E T_e^{(k)}(\lambda)\delta(t - t_e^{(k)}), \tag{14}$$

where I_E is the intensity emitted by the light source, $T^{(k)} = e^{-\mu_a^{(k)}(\lambda)d^{(k)}DPF^{(k)}(\lambda, d^{(k)})} = e^{\underline{n}^{(k)}}$ is the transmittance of the k^{th}-path, $t^{(k)} = \frac{||d^{(k)}||_1}{v}$ represents the time delay introduced by the propagation medium and the corresponding subscript *a* or *e* indicates if it is intracell or intercell propagation.

Furthermore, when the rays from the light source are discretized into *K* individual paths, they will traverse through *N* cells which are aligned between the transmitter and the receiver. Intuitively, all the corresponding impulse responses contributing to the received signal can be obtained by (14). Furthermore, (14) can be expressed in detailed by substituting

the transmittance by the exponential equation as follows

$$\begin{bmatrix} h_a^{(1)} \\ h_e^{(1)} \\ h_a^{(2)} \\ h_e^{(2)} \\ \vdots \\ h_a^{(K)} \\ h_e^{(K)} \end{bmatrix} = I_E \cdot e^{\underline{\eta}^T} \begin{bmatrix} \delta(t - \frac{||\underline{d_a^{(1)}}||_1}{v_a}) \\ \delta(t - \frac{||\underline{d_e^{(1)}}||_1}{v_e}) \\ \delta(t - \frac{||\underline{d_a^{(2)}}||_1}{v_a}) \\ \delta(t - \frac{||\underline{d_e^{(2)}}||_1}{v_e}) \\ \vdots \\ \delta(t - \frac{||\underline{d_a^{(K)}}||_1}{v_a}) \\ \delta(t - \frac{||\underline{d_e^{(K)}}||_1}{v_e}) \end{bmatrix},$$

where η represents the matrix product of the absorption coefficient, the distance and the DPF, v is the light velocity in the medium, and subscript a or e indicates if the path is intra or intercell propagation, respectively. The velocity value can be obtained by $v = \frac{c}{n}$, where c is the light speed in vacuum and n is the refractive index of the medium. Therefore, the matrix product η is further substituted by the multiplication of the absorption coefficient, distance, and DPF and represented as

$$\underline{\eta} = \begin{bmatrix} \eta_a^{(1)} \\ \eta_e^{(1)} \\ \eta_a^{(2)} \\ \eta_e^{(2)} \\ \vdots \\ \eta_a^{(K)} \\ \eta_e^{(K)} \end{bmatrix} = \begin{bmatrix} -\mu_a^{(c)} \sum_{n=1}^{N} d_a^{(1,n)} \\ -\mu_a^{(u)} \sum_{n=1}^{N+1} d_e^{(1,n)} \\ -\mu_a^{(c)} \sum_{n=1}^{N} d_a^{(2,n)} \\ -\mu_a^{(u)} \sum_{n=1}^{N+1} d_e^{(2,n)} \\ \cdots \\ -\mu_a^{(c)} \sum_{n=1}^{N} d_a^{(K,n)} \\ -\mu_a^{(u)} \sum_{n=1}^{N+1} d_e^{(K,n)} \end{bmatrix}^T \begin{bmatrix} DPF_a^{(1)} \\ DPF_e^{(1)} \\ DPF_a^{(2)} \\ DPF_e^{(2)} \\ \vdots \\ DPF_a^{(K)} \\ DPF_e^{(K)} \end{bmatrix}.$$

where μ_a is the absorption coefficient and the superscript (c) or (u) indicates either the neuron or the brain tissue, respectively.

V. Frequency Domain Analysis

In optogenetics, the wavelength that is used for the neuron stimulation is based on the visible 450-480 nm blue light, and this is the same wavelength that is used for the light communication between the WiOptND devices in our proposed model. The communication is established through light propagation that is represented as a short Gaussian shaped pulse. The Gaussian shaped pulse is the product of a cosine function and a Gaussian envelope function. For a light wave, the Gaussian pulse can be expressed as [23]

$$E_t = Re\{E_0 e^{-4ln(2)\left(\frac{t}{\tau}\right)^2 + i\omega_0 t}\} \tag{15}$$

where E_t and E_0 are the electric field with respect to time $t = 0$, respectively, ω_0 is the angular frequency of the light wave, and τ is the Full-Width at Half-Maximum (FWHM) pulse duration. On the receiver side, the time delay is added to the pulse waveform and it is formulated as

$$E_r = Re\{\gamma E_0 e^{-4ln(2)\left(\frac{t-t_d}{\tau}\right)^2 + i\omega_0(t-t_d)}\}, \tag{16}$$

where t_d denotes the time delay caused by the propagation path and $\gamma = \left(\frac{r_E}{r_D}\right)^2$ is the area (proportional to the square of radius) ratio due to the focusing effect, r_E is the radius of the light source and r_D is at the detector [12]. The result from the convolution series of the channel impulse response presented in (12) can also be obtained by analysing the Fourier transforms of the transmitted signal, $\mathcal{F}(E_t)$, and the received signal $\mathcal{F}(E_r)$. The channel impulse response can be obtained by applying the inverse Fourier transform of the division, and is represented as

$$h(t; d, \lambda) = \mathcal{F}^{-1}(H(f; d, \lambda) = \mathcal{F}^{-1}\left(\frac{\mathcal{F}(E_r(t; d, \lambda)}{\mathcal{F}(E_t(t; d, \lambda)}\right). \tag{17}$$

Based on (15) and (16), we can observe that the input and output relationship is heavily dependent on the delay caused by the propagation medium characteristics. To obtain this impulse channel characterisation, which correlates with the delay and focusing factors, we further process the transmitted and received time domain signals in the frequency domain.

VI. Numerical Analysis

In this paper, the light propagation is simulated using MATLAB, where the simulator generates geometrical rays that propagate through both the brain tissue as well as the three different shapes of neurons. Our approach used for the light propagation modeling is based on a ray tracing algorithm. Algorithm 1 presents an example for the fusiform cell ray tracing process, and similar algorithms are also developed for the spherical and pyramidal cells based on their geometrical properties. This function is iteratively executed and combined with the ray tracing by applying the focusing parameter γ from (16), which is determined by the illuminated detection area. Table I lists all the parameters that was used in the MATLAB simulation.

A. Path Loss and Geometrical Gain

The light wave traversing in the biological tissue experiences attenuation as discussed in Sec. II. The attenuation is mainly due to the optical properties of all the biological components in the cell medium. However, the fusiform and the spherical cells focuses the light rays as it enters into the cytoplasm, and this is due to the changes in the refractive index. This focusing effect is further increased when the light propagates into the nucleus, and once again this is due to the differences in the refractive indexes of the medium [11]. Fig. 4 shows the effect of the focusing ratio and illumination radius which contribute to the overall gain of the light intensity. This can be observed in the rise of the illumination as the light propagates through certain cells and then divergence occurs leading to reduction in the illumination.

TABLE I
SIMULATION PARAMETERS

Parameter	Value [Unit]	Description
λ	456 $[nm]$	Visible blue light wavelength
n_c	1.36	Refractive index of the cell [24]
n_t	1.35	Refractive index of the tissue
$\mu_a^{(c)}$	0.9 $[/mm]$	Cell absorption coefficient [25]
$\mu_s^{\prime(c)}$	3.43 $[/mm]$	Cell reduced scattering coefficient
$\mu_a^{(u)}$	20 $[/mm]$	Tissue absorption coefficient [26]
$\mu_s^{\prime(u)}$	1.43 $[/mm]$	Tissue reduced scattering coefficient
τ	1 $[fs]$	FWHM pulse duration

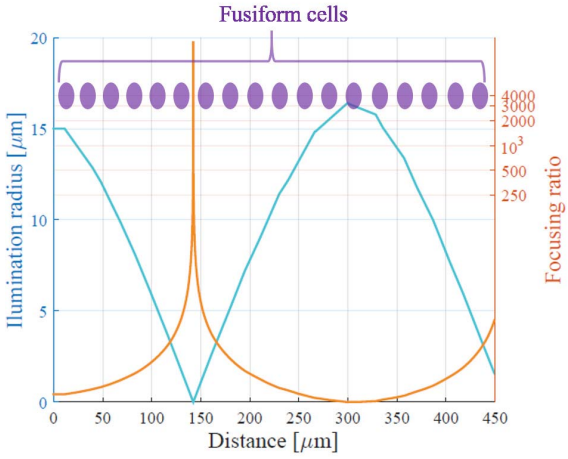

Fig. 4. Illumination radius ($h_2/h_3/h_4$) and focusing ratio γ for eighteen fusiform neurons.

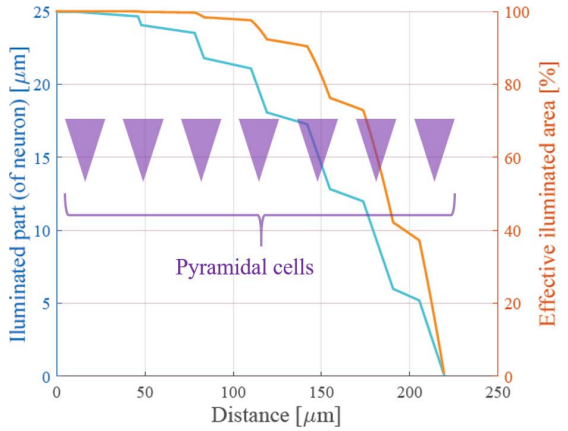

Fig. 5. Illumination height ($h_2/h_3/h_4$) and effective illumination area for seven pyramidal neurons.

The focusing behaviour is not found in the pyramidal shaped cell. Fig. 5 presents the illumination and shows that it gradually reduces due to the divergence of the light path away from the line of cells. This is solely due to the geometrical structure of the cell, as illustrated in Fig. 6.

Fig. 7 shows the path loss within the brain tissue for the three different neurons, where the transmitter and receiver is separated by 450 μm. In case of the pyramidal cells, the ray deviation due to the geometrical refraction causes the gradient change (marked by yellow shade). The deviation indicates that the light does not penetrate through the remaining neurons along its path, and this is because for the fusiform cells there are eighteen neurons along the propagation path, while the pyramidal cells has seven neurons due to the light path divergence.

B. Time and Frequency Analysis

We compare the delay and channel impulse response for the light propagation and determine how it gets impacted from the geometrics of the three neuron cells. The simulation of the light path was for one dimension of 18 neurons that are linearly positioned along the wave propagation direction. In all cases, the receiver is located at a distance of 450 μm from the transmitter.

Fig. 8 shows both the time and frequency domain analysis. In our simulation, one femtosecond Gaussian light pulse is transmitted from a source which is located at 5 μm from the first cell on the path. The signal is analyzed at the receiver, and the peak frequency of the transmitted signal is approximately 500 THz. From the ray tracing analysis, the delay can be characterized by integrating all the incident rays at 450 μm distance from the transmitter.

Fig. 8 shows the channel impulse response of the one-dimensional neuron cells and is obtained by FFT and IFFT as explained in Sec. V. As shown in Fig. 8, the channel impulse response exhibits correlation with the power delay profile in terms of its peak magnitude of the received signal in the time domain. The light propagating through the fusiform cells experiences higher delay compared to the other two cell types since the light propagates mostly though the one dimensional array of neural tissue. In general, the speed of light in the brain tissue is faster than in the neuron because of the smaller refractive index. On the other hand, the light is absorbed less by the neurons due to its lower absorption coefficient, resulting in lower signal attenuation magnitude. The segmented time delays found in the pyramidal cells is caused by the ray leakages that occurs intermittently along the tissue. This phenomenon does not occur in two other type of cells since most of the ray propagation in two other cells are maintained along the straight path, even though there will be minor divergences and leakages along the path.

Fig. 9 depicts the channel impulse response for the three cell shapes with respect to the number of cells along the propagation path. It is obvious that the number of cells has a significant effect on the time of arrival of the signals since the refractive index of the cell is higher, resulting in slower light propagation velocity. The magnitude of the signal is dictated by the attenuation medium properties for all cell types and focusing parameters for both fusiform and spherical cells,

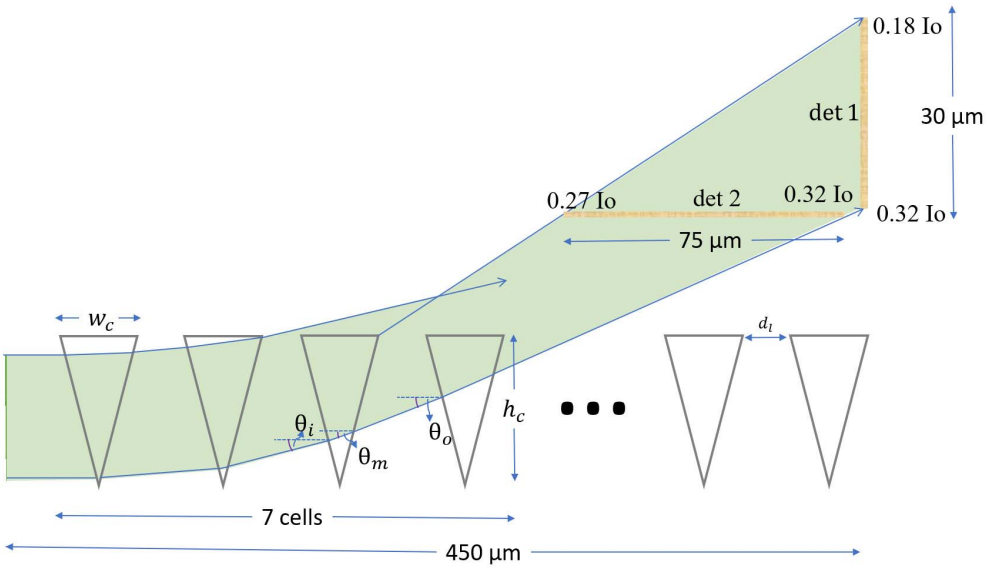

Fig. 6. Light path deviation along an array of pyramidal cells due to the geometric shape.

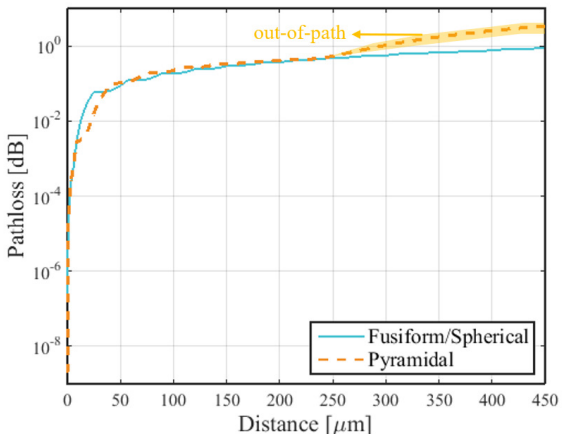

Fig. 7. Light propagation path loss for the distance of 450 μm between the transmitter and receiver with 18 cells in between.

which is determined in (16). The difference between the three cells is solely due to the geometry which affects the distance of the focus point $foc(\theta_F, x_F)$, focusing parameter γ, and the ratio of the total light propagation distance in the cell $\overline{d_a}$ and the brain tissue $\overline{d_e}$. The impulse response for the pyramidal cells increases gradually as the number of cell goes higher due to less traveled distance, before the light is diverged leading to no focusing effect.

C. Power Characteristics on the Receiver

On the receiver, the total received signal is the result of the superposition of the light rays that arrive at the receiver surface. Fig. 10 shows the peak transmitted and received pulse shapes of different cell types as a result of superposition which is based on the time domain analysis elaborated in Sec. IV. Furthermore, the received signal power difference for those cells is mainly caused by the propagation distance ratio of the brain tissue for each path and the neurons, as well as the geometrical gain for each cell shape.

The previous results have shown that there are different propagation paths depending on the cell types, and this has an impact on how the detector on the receiver is designed. All the cells along the one-dimensional neural tissue contributes to the delay and attenuation of the light signal. Consequently, the geometry and the amount of the traversed cells also has an impact on the received power characteristics. Fig. 11 shows the received power characteristics on the detector of the receiver for both the fusiform and pyramidal cells. In the case of the fusiform cell's receiver detector, the width is 40 μm, while in the case of the pyramidal it is 30 μm. In the case of the fusiform cells (Fig. 11 (a)), the power concentration is located in the middle of the detector and this is in-line to the propagation direction where the cells are aligned. This is directly linked to the focusing phenomenon that occurs in both fusiform and spherical cells. In order to detect all the transmitted rays, the detector height should be equal to the height of the cell, h_c, which is 30 μm used in our simulation. On the other hand, different characteristics is observed for the pyramidal cells where gradual power change occurs in stages and it is also segmented (Fig. 11 (b)). While the height configuration of the detector used is 30 μm, this parameter is dependent on the cell configuration (the number of traversed cells). The segmented phenomenon occurs due to leaking rays effect discussed in the earlier section. Unlike the fusiform and spherical cells, which causes power concentration at the centre of the detector, in the case of the pyramidal cells, the light rays that traverses through more cells experiences less attenuation as well as deviations from the original propagation line. Therefore, for both fusiform as well as spherical cells, the detector should be positioned at the center of the propagation line. In the case of the pyramidal cells, there are two ways for positioning the detector. As illustrated in Fig. 6, there are both

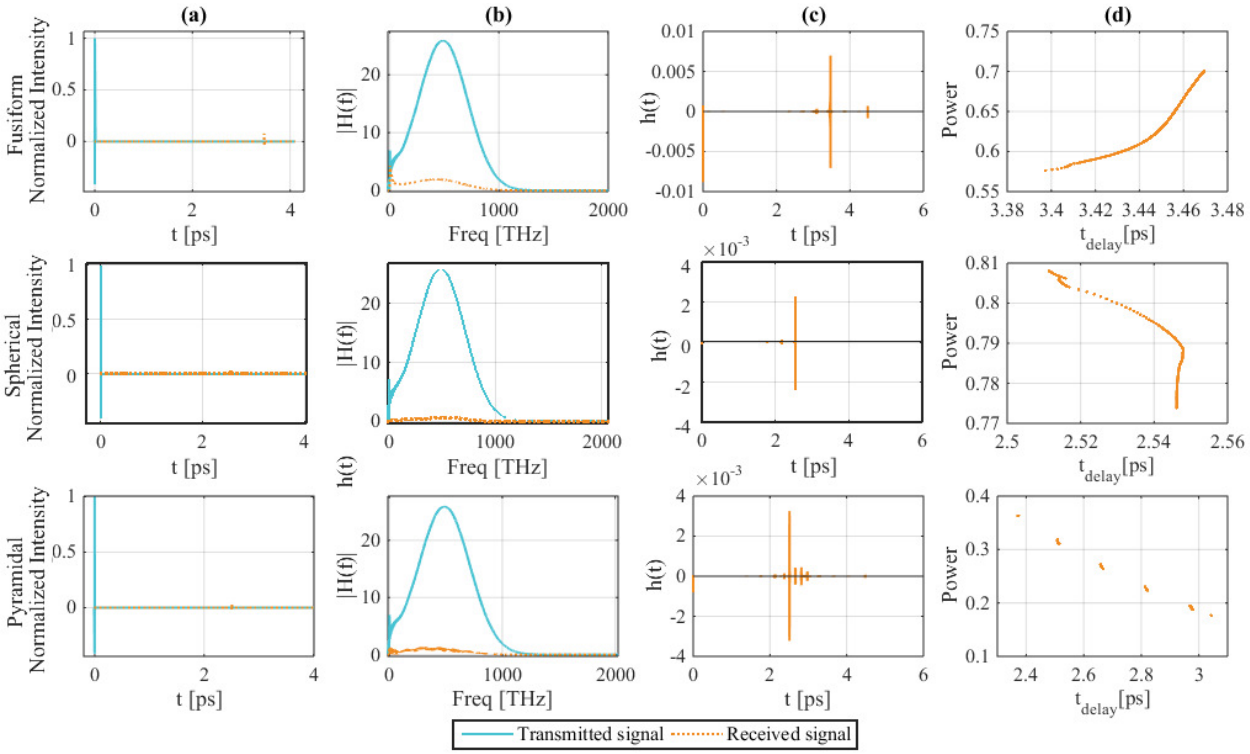

Fig. 8. Time and frequency analysis of light propagation along fusiform, spherical, and pyramidal cells. (a) The normalized intensity of the transmitted and the received signals in the time domain, (b) Absolute value of the transmitted and the received signal in the frequency domain, (c) Channel impulse response, and (d) Power delay profile.

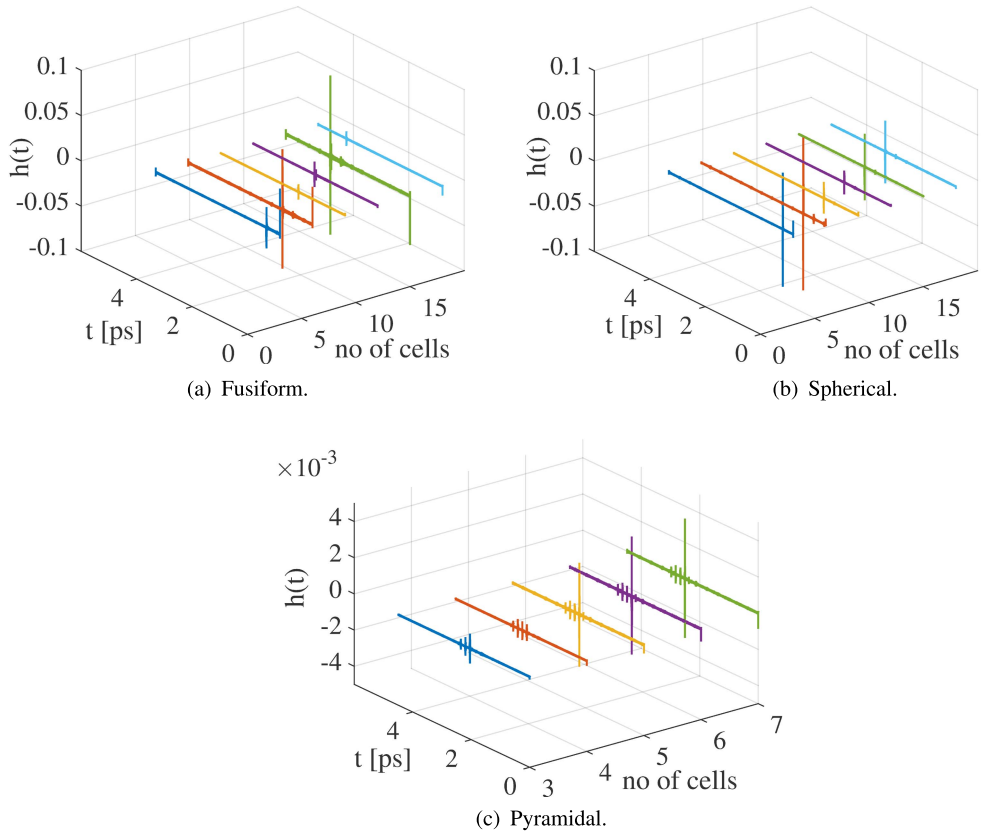

Fig. 9. Channel impulse response $h(t)$ for three shapes of cells with variable number of cells along the propagation path.

horizontal and vertical orientations. The horizontal orientation provides better benefit since the propagation distance can be minimized, but the detected intensity is higher than in the vertical orientation.

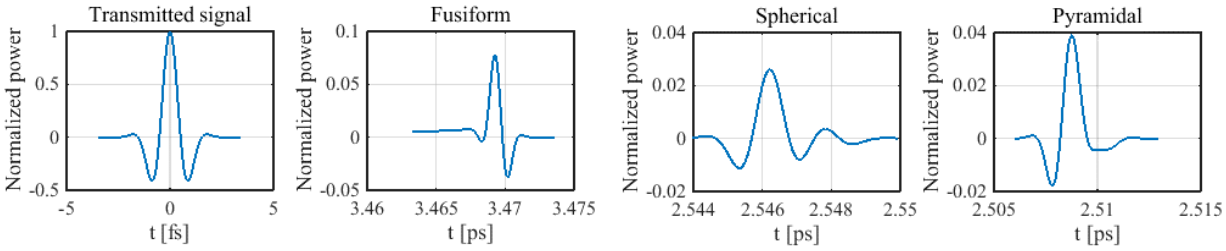

Fig. 10. The highest magnitude pulse shapes of the transmitted signal (gaussian short pulse) and the received signals after 450 μm propagation through one dimensional array of cells.

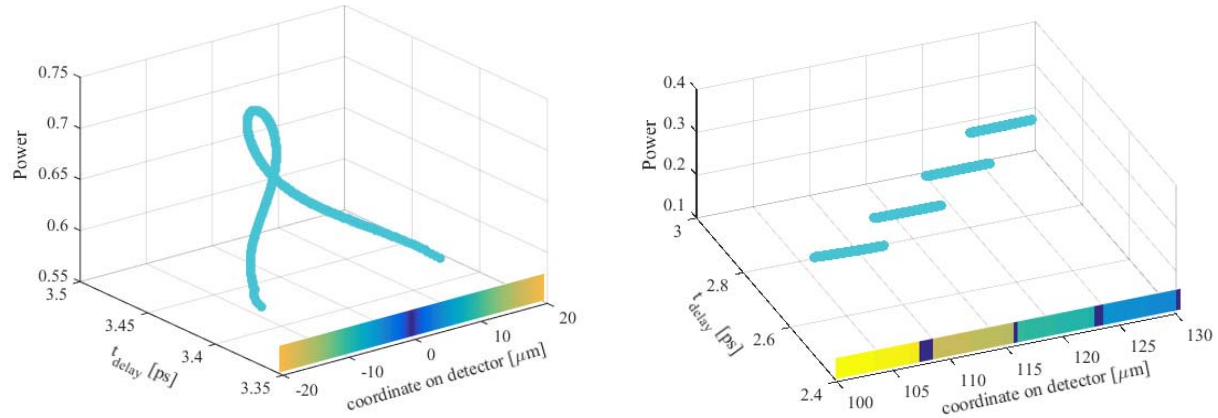

(a) Fusiform. (b) Pyramidal.

Fig. 11. Normalized power of light ray with respect to the transmission delay when it arrives at a certain coordinate of a detector for (a) Fusiform cells, and (b) Pyramidal cells.

VII. Conclusion

While light has been investigated for neural stimulation based on the concept of optogenetics, this paper addresses the light propagation from a nano-scale light source that can be used for communication between the WiOptND devices. The analysis presented in this paper discussed the important factors that affect the light propagation through neurons and brain tissue, namely the medium optical properties (μ_a and μ_s) and the geometric structures of the cells. The cells investigated in this paper are fusiform, spherical, and pyramidal neurons. An interesting effect is the distance and the number of the cells along the propagation axis, which affects the path loss as well as the geometrical gain.

The channel impulse response of the light propagating along the neurons have an interesting behaviour. In the time domain, the delay of the simulated system can be observed when the light pulse is sufficiently short (femto second) since the delay is in the pico second level. This means that for longer pulses, the delay is insignificant. The time delays for the fusiform, spherical, and pyramidal are approximately 3.4, 2.5 and 2.7 ps, respectively. Additionally, radial-based geometries (fusiform and spherical) exhibit alternating high and low amplitude, while pyramidal tends to exhibit increasing amplitude signal level as the distance increases due to the path traversing through neurons more than the brain tissue. However, all shapes experience increasing delay as the distance increases. In terms of the frequency domain, the propagated signal does not experience any change in its frequency range. Both the time and frequency analysis exhibit 35%, 20%, and 65% attenuation in the signal power for the fusiform, spherical, and pyramidal cells, respectively. Moreover, the shape of the received signal is governed mainly by the geometrical shape of the cell where the diffraction causes the change in light directions for the pyramidal cell. The radial-based-geometry cell exhibited radial pattern in the power gradient at the receiver. In the case of the pyramidal cells, the position of the receiver is very important to obtain maximum light intensity for accurate detection. Our analysis found that the light intensity at the detector greatly varies across the area of the detector.

Analysis in this paper has shown that light propagation as a mode for communication between WiOptND implantable devices in the brain is a viable solution. The impulse response shows how the light propagation behaviour varies with the number of cells and how this can impact on the area design of the detector. This can lead to WiOptND devices that can be placed in various layers of the cortical column of the cortex, and coordinate their stimulation sequences of the neurons. The result of this research is a new form of Brain-Machine Interface that allows control and stimulation at single-neuron level, leading to new forms of treatments for neurodegenerative diseases.

Appendix
Ray Tracing Algorithm for Fusiform Cell

This algorithm processes the optical properties of the medium (n_c, n_t), physical properties of the cell (r_c, d_c), and coordinates/direction of the incoming ray (x_2, h_2, θ_i).

Algorithm 1 Ray Tracing for Fusiform Cell

Require:

n_c, n_t (refractive indices of cell and tissue)
r_c (the radius of the cell)
x_2 (the ray x-coordinate of the previous cell)
h_2 (the radius of incoming illumination)
d_c (the distance between cells)
θ_i (the angle of the incoming ray)

Ensure:

$foc(\theta_F, x_F)$ (the distance and angle of focus point)
$l_i(x_3', h_3)$ (the coordinate of the incoming ray),
$l_o(x_4, h_4)$ (the coordinate of the outgoing ray)
$\theta_i^{(2)}$ (the ray propagation angle in the cell)

1: CALCULATE x_2' ▷ x_2' = x_2 measured from the 1^{st} surface,

$$x_2' = (d_c + 2r_c) - x_2$$

2: CALCULATE x_3, h_3 ▷ x_3, h_3 = the coordinate where the ray hits the 1^{st} surface,

$$m_2 = tan(180^o - \theta_i)$$
$$h_3 = \begin{bmatrix} m_2^2 + 1 \\ 2m_2(h_2 + m_2 x_2') \\ (h_2 + m_2 x_2')^2 - r_c^2 \end{bmatrix}^T \begin{bmatrix} x_3^2 \\ x_3 \\ 1 \end{bmatrix}$$

3: CALCULATE$\theta_i^{(1)}$ ▷ the incoming angle with respect to normal line of the 1^{nd} surface

$$\theta_i'^{(1)} = arctan\Big(\frac{h_3}{|x_3|}\Big) - \theta_i^{(1)}$$

4: CALCULATE$\theta_o^{(1)}$ ▷ the refracted angle due to 1^{st} surface

$$\theta_o^{(1)} = arcsin\Big(\frac{n_t sin(\theta_i'^{(1)})}{n_c}\Big)$$

5: CALCULATEx_3, $\theta_o^{(1)}$ ▷ with respect to 2^{nd} surface

$$x_3' = 2r_c - (d_c + |x_3|)$$
$$\theta_i^{(2)} = \theta_i^{(1)} + (\theta_i'(1) + \theta_o^{(1)})$$

6: CALCULATEx_4, h_4 ▷ the coordinate where the ray hits the 2^{nd} surface

$$m_3 = tan(-\theta_i^{(2)})$$
$$h_4 = \begin{bmatrix} m_3^2 + 1 \\ 2m_3(h_3 + m_3 x_3') \\ (h_3 + m_3 x_3')^2 - r_c^2 \end{bmatrix}^T \begin{bmatrix} x_4^2 \\ x_4 \\ 1 \end{bmatrix}$$

7: CALCULATE$\theta_o^{(2)}$ ▷ the refracted angle due to 2^{nd} surface

$$\theta_o^{(2)} = arcsin\left(\frac{n_c}{n_t} sin\Big(arctan\Big(\frac{h_4}{x_4}\Big) + \theta_i^{(2)}\Big)\right)$$

8: CALCULATEx_F ▷ the focus distance

$$\theta_F = \theta_o^{(2)} - arctan\Big(\frac{h_4}{x_4}\Big)$$
$$m_4 = tan(\theta_F)$$
$$x_F = \frac{m_4 x_4 - h_4}{m_4}$$

It generates the focus angle/coordinates ($foc(\theta_F, x_F)$) and propagation direction/coordinates inside the cell ($l_i(x_3', h_3)$, $l_o(x_4, h_4)$, $\theta_i^{(2)}$). For a series of cells, the iterative execution of this algorithm is required.

REFERENCES

[1] I. F. Akyildiz and J. M. Jornet, "Electromagnetic wireless nanosensor networks," *Nano Commun. Netw.*, vol. 1, no. 1, pp. 3–19, Mar. 2010.

[2] I. F. Akyildiz, F. Brunetti, and C. Blázquez, "Nanonetworks: A new communication paradigm," *Comput. Netw.*, vol. 52, no. 12, pp. 2260–2279, Aug. 2008.

[3] N. A. Abbasi, D. Lafci, and O. B. Akan, "Controlled information transfer through an *in vivo* nervous system," *Sci. Rep.*, vol. 8, no. 1, p. 2298, Dec. 2018.

[4] H. Ramezani and O. B. Akan, "Impacts of spike shape variations on synaptic communication," *IEEE Trans. Nanobiosci.*, vol. 17, no. 3, pp. 260–271, Jul. 2018.

[5] M. Veletic, P. A. Floor, Y. Chahibi, and I. Balasingham, "On the upper bound of the information capacity in neuronal synapses," *IEEE Trans. Commun.*, vol. 64, no. 12, pp. 5025–5036, Dec. 2016.

[6] G. E. Santagati and T. Melodia, "A software-defined ultrasonic networking framework for wearable devices," *IEEE/ACM Trans. Netw.*, vol. 25, no. 2, pp. 960–973, Apr. 2017.

[7] P. Johari and J. M. Jornet, "Nanoscale optical wireless channel model for intra-body communications: Geometrical, time, and frequency domain analyses," *IEEE Trans. Commun.*, vol. 66, no. 4, pp. 1579–1593, Apr. 2018.

[8] H. Elayan, P. Johari, R. M. Shubair, and J. M. Jornet, "Photothermal modeling and analysis of intrabody terahertz nanoscale communication," *IEEE Trans. Nanobiosci.*, vol. 16, no. 8, pp. 755–763, Dec. 2017.

[9] S. A. Wirdatmadja, M. T. Barros, Y. Koucheryavy, J. M. Jornet, and S. Balasubramaniam, "Wireless optogenetic nanonetworks for brain stimulation: Device model and charging protocols," *IEEE Trans. Nanobiosci.*, vol. 16, no. 8, pp. 859–872, Dec. 2017.

[10] A. Noel, D. Makrakis, and A. W. Eckford, "Distortion distribution of neural spike train sequence matching with optogenetics," *IEEE Trans. Biomed. Eng.*, vol. 65, no. 12, pp. 2814–2826, Dec. 2018.

[11] S. Wirdatmadja *et al.*, "Analysis of light propagation on physiological properties of neurons for nanoscale optogenetics," *IEEE Trans. Neural Syst. Rehabil. Eng.*, vol. 27, no. 2, pp. 108–117, Feb. 2019.

[12] S. Wirdatmadja, P. Johari, S. Balasubramaniam, Y. Bae, M. K. Stachowiak, and J. M. Jornet, "Light propagation analysis in nervous tissue for wireless optogenetic nanonetworks," *Proc. SPIE*, vol. 10482, Feb. 2018, Art. no. 104820R.

[13] V. V. Tuchin, "Tissue optics and photonics: Biological tissue structures," *J. Biomed. Photon. Eng.*, vol. 1, no. 1, pp. 3–21, Mar. 2015.

[14] C. Fang-Yen and M. S. Feld, "Intrinsic optical signals in neural tissues: Measurements, mechanisms, and applications," in *Proc. ACS Sym. Ser.*, vol. 963, 2007, pp. 219–235.

[15] J. D. Johansson, "Spectroscopic method for determination of the absorption coefficient in brain tissue," *J. Biomed. Opt.*, vol. 15, no. 5, 2010, Art. no. 057005.

[16] S. I. Al-Juboori, A. Dondzillo, E. A. Stubblefield, G. Felsen, T. C. Lei, and A. Klug, "Light scattering properties vary across different regions of the adult mouse brain," *PLoS ONE*, vol. 8, no. 7, Jul. 2013, Art. no. e67626.

[17] R. Renaud, C. Martin, H. Gurden, and F. Pain, "Multispectral reflectance imaging of brain activation in rodents: Methodological study of the differential path length estimations and first *in vivo* recordings in the rat olfactory bulb," *J. Biomed. Opt.*, vol. 17, no. 1, 2012, Art. no. 016012.

[18] F. Scholkmann and M. Wolf, "General equation for the differential pathlength factor of the frontal human head depending on wavelength and age," *J. Biomed. Opt.*, vol. 18, no. 10, Oct. 2013, Art. no. 105004.

[19] L. Chuye *et al.*, "Brain organoids: Expanding our understanding of human development and disease," in *Human Neural Stem Cells*. Cham, Switzerland: Springer, 2018, pp. 183–206.

[20] C. Von Economo, *Cellular Structure of the Human Cerebral Cortex*. Basel, Switzerland: Karger Medical and Scientific Publishers, 2009.

[21] T. Nguyen, "Total number of synapses in the adult human neocortex," *Undergraduate J. Math. Modeling: One+Two*, vol. 3, no. 1, p. 26, May 2013.

[22] S. P. Rodríguez, R. P. Jiménez, B. R. Mendoza, F. J. L. Hernández, and A. J. A. Alfonso, "Simulation of impulse response for indoor visible light communications using 3D CAD models," *EURASIP J. Wireless Commun. Netw.*, vol. 2013, no. 1, p. 7, Dec. 2013.

[23] C. Rulliere *et al.*, *Femtosecond Laser Pulses*. New York, NY, USA: Springer, 2005.
[24] A. Levinson and A. Serby, "The refractometric and viscosimetric indexes of cerebrospinal fluid," *Arch. Internal Med.*, vol. 37, no. 1, pp. 144–150, 1926.
[25] A. Yaroslavsky, P. Schulze, I. Yaroslavsky, R. Schober, F. Ulrich, and H. Schwarzmaier, "Optical properties of selected native and coagulated human brain tissues in vitro in the visible and near infrared spectral range," *Phys. Med. Biol.*, vol. 47, no. 12, p. 2059, 2002.
[26] N. Bosschaart, G. J. Edelman, M. C. G. Aalders, T. G. van Leeuwen, and D. J. Faber, "A literature review and novel theoretical approach on the optical properties of whole blood," *Lasers Med. Sci.*, vol. 29, no. 2, pp. 453–479, Mar. 2014.

Stefanus Wirdatmadja received the B.Sc. degree in electrical engineering from Universitas Indonesia, Depok, Indonesia, in 2005, and the M.Sc. degree in wireless communication circuits and system from the Tampere University of Technology, Finland, in 2015. He is currently pursuing the Ph.D. degree with the Department of Electronics and Communications Engineering, Tampere University, Finland. His current research interests include Internet of BioNanoThings, molecular communications, and bio nanoscience.

Josep Miquel Jornet (Member, IEEE) is currently an Associate Professor with the Department of Electrical and Computer Engineering, Northeastern University, the Director of the Ultrabroadband Nanonetworking (UN) Laboratory, and a member of the Institute for the Wireless Internet of Things, NU. His current research interests are in Terahertz-band communication networks, nanophotonic wireless communication, wireless nano-bio-sensing networks, and the Internet of Nano-Things. In these areas, he has coauthored more than 120 peer-reviewed scientific publications, including one book and three U.S. patents. Since 2016, he has been the Editor in Chief for Nano Communication Networks (Elsevier) Journal.

Yevgeni Koucheryavy (Senior Member, IEEE) received the Ph.D. degree from Tampere University of Technology (TUT), Finland, in 2004. He is currently a Full Professor with the Unit of Electrical Engineering, TUT. He has authored numerous publications in the field of advanced wired and wireless networking and communications. He is an Associate Technical Editor of the *IEEE Communications Magazine*.

Sasitharan Balasubramaniam (Senior Member, IEEE) received the B.E. degree in electrical and electronic engineering and the Ph.D. degree from the University of Queensland, in 1998 and 2005, respectively, and the M.E. degree in computer and communication engineering from the Queensland University of Technology, in 1999. He is currently the Director of Research with the Telecommunication Software and Systems Group, Waterford Institute of Technology, Ireland. He is also on the steering board committee of ACM NanoCom, which he co-founded, and an Associate Editor for IEEE TRANSACTIONS ON MOLECULAR, BIOLOGICAL, AND MULTI-SCALE COMMUNICATIONS, IEEE LETTERS OF THE COMPUTER SOCIETY, *Nano Communication Networks* (Elsevier), and Digital Communications and Networks (Elsevier). In 2018, he was IEEE Nanotechnology Council Distinguished Lecturer.